Letter

Machine learning electron-phonon interactions in two-dimensional semiconducting materials: The case of zero-point renormalization

Anubhab Haldar,[1,*] Quentin Clark,[1,2,*] Marios Zacharias,[3] Feliciano Giustino,[4,5] and Sahar Sharifzadeh[1,6,†]

[1]Department of Electrical and Computer Engineering, Boston University, Boston, Massachusetts, USA
[2]Department of Philosophy, Boston University, Boston, Massachusetts, USA
[3]Université de Rennes, INSA Rennes, CNRS, Institut FOTON, Rennes, France
[4]Oden Institute for Computational Engineering and Sciences, The University of Texas, Austin, Austin, Texas, USA
[5]Department of Physics, The University of Texas, Austin, Austin, Texas, USA
[6]Division of Materials Science and Engineering, Boston University, Boston, Massachusetts, USA

(Received 12 March 2024; accepted 24 September 2024; published 11 October 2024)

We utilize first-principles theory to investigate the role of electron-phonon interactions within a dataset of monolayer materials. Using density functional theory to describe excited-state transitions and the special displacement method to describe the role of phonons, we analyze the relationship between simple physical observables and electron-phonon coupling strength. For over 100 materials, we compute the band gap renormalization due to zero-point vibrational (ZPR) motion as a measure of electron-phonon interactions and train a machine learning model based on physical parameters. We demonstrate that the strength of electron-phonon interactions is highly dependent on the band gap, dielectric constant, and degree of ionicity, all of which can be physically justified. We then apply this model to 1302 2D materials, predicting the ZPR, which for five randomly selected materials tested agree well with the first-principles predictions. This work provides an approach for quantitatively predicting the ZPR as a measure of electron-phonon interactions in 2D materials.

DOI: 10.1103/PhysRevMaterials.8.L101001

Introduction. Due to their reduced dimensionality and screening environment, electron-phonon (EPH) interactions in two-dimensional (2D) materials can be particularly amplified [1–6]. These interactions can be exploited for technological applications [7–10] or may need to be minimized for improved material functionality (i.e., improved mobility [11]). As such, understanding the microscopic origins of EPH interactions is crucial for comprehending the functional behavior of 2D materials. Developing a physical intuition for EPH is difficult because of the structural and electronic complexity of these materials. First-principles theory can, in principle, accurately describe EPH [12–31]. However, first-principles theory is limited to studying a few materials systems because of the computational cost, and thus, it is difficult to systematically study a series of materials.

Machine learning (ML) can aid in the prediction of EPH and its impact on materials properties by extracting physical intuition and providing quantitative models based on data [32,33]. ML has been particularly relevant for predicting new superconductors, for which the magnitude of the EPH coupling element determines the expected superconducting temperature [34–37]. For hybrid metal-organic perovskites, another class of materials for which EPH interactions play a key role, ML has been utilized to understand the relationships between atomic vibrations with the excited-state lifetime [38], degradation [39], and thermoelectric performance [40].

In this study, we combine the special displacement method (SDM), a recently formalized approach for including EPH interactions [16,30] with an extra random tree (ERT) ML model to understand key descriptors associated with electron-phonon interactions, and specifically band gap renormalization, in 2D materials. The SDM is a relatively simple approach that describes transitions among coupled electron-nuclear quantum states in the adiabatic approximation, allowing the generation of greater than 100 datapoints to train the model, while ERT provides an ML model that is robust against overfitting of small datasets, and has been applied to materials data previously [41].

We extract 128 materials from the MC2D database [42] and study the zero-point renormalization (ZPR) of the band gap computed within density functional theory (DFT) as a measure of EPH interactions. In order to understand the relationship between physical observables and ZPR, we build an ERT model fit with nine features that are motivated by physical observables, and analyze the most important features using a SHAPley analysis [43], a model explainability technique that quantifies how individual features of each material impact the ZPR. Similar models have been applied for other materials applications [41,44–48] because of the robustness of random forest models and SHAPley analysis, but this is the first such application to electronic structure that we are aware of. We apply this model to 1302 materials from the C2DB database [49], producing a list of predicted ZPR that we expect to provide qualitatively accurate trends.

Results. In the SDM, the effect of EPH coupling is incorporated in *ab initio* calculations by displacing the nuclei

*These authors contributed equally to this work.
†Contact author: ssharifz@bu.edu

away from their static-equilibrium positions. As described in Refs. [16,30], the influence of phonons is incorporated into the atomic structure of the material and an excited-state approach is applied to describe the averaged temperature-dependent excitation. The special displacements [30] are a linear combination of the phonon eigenvectors with coefficients determined by the associated mean square displacements of the atoms. Previously [50,51], we applied the SDM to understand the impact of phonons on excitonic properties of low-dimensional materials.

The ZPR of the energy levels obtained using SDM is equivalent, up to second order in normal coordinates, to the perturbative expression derived from the adiabatic Allen-Heine theory (see Methods of [52]). The renormalization of band energies is derived as [17,53],

$$\Delta\varepsilon_n = \sum_{m\neq n,\nu}\left[\frac{|g_{mn,\nu}|^2}{\varepsilon_n-\varepsilon_m}+\frac{1}{2}h_{n\nu}\right]l_\nu^2, \tag{1}$$

where n, m are indices for the electron states with energies $\varepsilon_n, \varepsilon_m$. The zero-point displacement amplitude associated with the phonon mode of frequency ω_ν is given by $l_\nu = [\hbar/(2M_0\omega_\nu)]^{1/2}$, where M_0 represents the proton mass. The Fan-Migdal and Debye-Waller EPH matrix elements are represented by $g_{mn,\nu}$ (g hereon) and $h_{n\nu}$ and can be computed as

$$g_{mn,\nu} = \langle u_m|\frac{\partial v_{\mathrm{KS}}}{\partial x_\nu}|u_n\rangle, \quad h_{n\nu} = \langle u_n|\frac{\partial^2 v_{\mathrm{KS}}}{\partial x_\nu^2}|u_n\rangle. \tag{2}$$

Here, v_{KS} is the Kohn-Sham (KS) potential, x_ν are the normal mode coordinates, and $|u_m\rangle$, $|u_n\rangle$ are the cell-periodic part of the electron eigenstates. We stress that since the SDM relies on nonperturbative supercell calculations, higher-order EPH self-energy corrections are included automatically in the evaluation of the ZPR. However, the SDM misses corrections arising from nonadiabatic effects [54], long-range Fröhlich couplings [20,55], and the tadpole self-energy due to the formation of polarons [56,57]. Fröhlich electron-phonon couplings within ionic materials, in particular, are only captured partially within the SDM due to the finite size of the supercell. However, we expect this problem to be less significant in 2D materials where computing Fröhlich electron-phonon matrix elements do not require fine phonon samplings [58]. This is confirmed by direct calculations of the temperature-dependent bandgap renormalization in monolayer MoS_2, for which the SDM yields very good agreement with experiment [30].

The goal of this study is to understand Eq. (1) without the calculation of expensive first-principles quantities. By inspection of Eq. (2), we can qualitatively determine the physical parameters that are important for band gap renormalization. In particular, the strength of the EPH coupling depends on the electronic screening and on the amplitude of the atomic vibrations. In turn, these quantities scale with the dielectric constant, atomic masses, and phonon frequencies. In fact, atomic masses and mean phonon frequencies have recently been shown to correlate with zero-point renormalization for 18 inorganic compounds [31]. We also expect that the ionicity of bonds will impact the polar EPH coupling and to also contribute to the dielectric constant. While the EPH coupling strength is expected to scale with these physical parameters, as

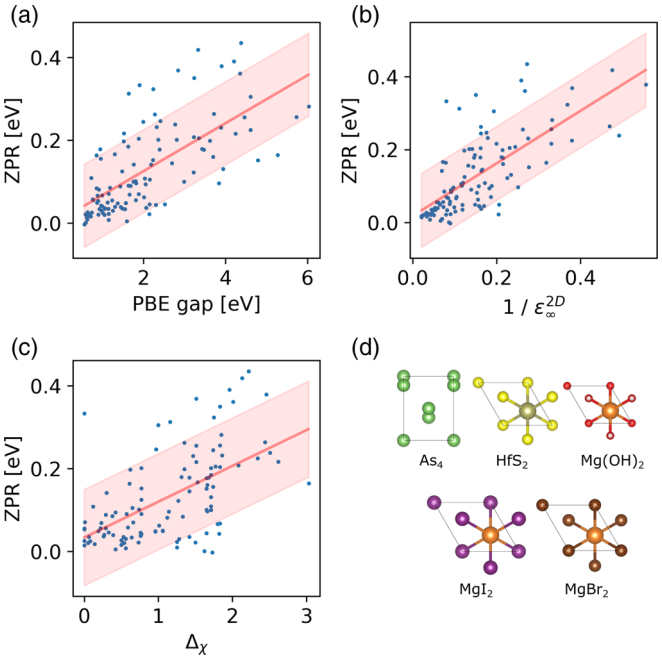

FIG. 1. Dependence of the ZPR on (a) DFT-PBE gap, (b) in-plane electronic dielectric constant, and (c) ionicity. Linear fit to the data is shown via a red line with twice the standard deviation of the residual error associated shown in the shaded region. The slope of the fitted line is 0.06, 0.72, and 0.09 for (a)–(c), respectively. (d) Atomistic geometries of a few representative systems in the training database as shown in Table I.

the material complexity increases, the interplay between these parameters is not clear, e.g., the case of compound semiconductors. In addition, this physical intuition does not provide quantitative trends, motivating the following data driven approach.

Figure 1 displays the correlation between three physical parameters and ZPR for the full dataset of materials studied computed within the Quantum Espresso package [59–62] employing the Perdew, Burke, and Ernzerhof (PBE) [63] exchange-correlation functional. We find a positive correla-

TABLE I. Relationship between ZPR and physical features defined in the text for five randomly selected materials from Ref. [42]. Qualitative correlation between features and ZPR for these materials are noted.

	As_4	HfS_2	$MgBr_2$	MgI_2	$Mg(OH)_2$	Correlation with ZPR
ZPR [eV]	0.025	0.030	0.15	0.20	0.42	–
E_g [eV]	0.74	1.25	4.79	3.62	3.33	Positive
$\epsilon_\infty^{2D}[\epsilon_0]$	22	9.9	3.6	4.7	2.1	Negative
$\overline{N}$ [1/Å^2]	0.23	0.26	0.23	0.20	0.57	Uncorrelated
ρ_{2D} [amu/Å^2]	17.2	21.3	14.2	18.6	6.7	Uncorrelated
$\overline{M}$ [amu]	74.9	80.9	61.4	92.7	11.7	Negative
$\Delta\chi$	0	1.28	1.65	1.35	2.13	Positive
ΔZ^* [q_e]	0	10.0	3.7	3.8	3.5	Uncorrelated
$\overline{\omega}$ [cm^{-1}]	82	205	99.5	71	277	Uncorrelated
ω_1 [cm^{-1}]	83	206	100	71	278	Uncorrelated

tion between the ZPR and equilibrium structure gaps with a slope of 0.06 [Fig. 1(a)], indicating that the gap is on-average reduced by 6% due to the presence of phonons. Within the Penn model, the average band gap ($\langle E_g \rangle$) and the static dielectric constant (ϵ) share an inverse relationship [64,65]; thus, we may expect this correlation to the gap will lead to an inverse relationship to ZPR as is shown in Fig. 1(b). For weak screening materials, $\epsilon < 4$, the renormalization is significant, consistent with the expectation that electronic screening is one of the dominant physical variables that influences the magnitude of the zero-point renormalization in 2D materials. For mid-range values of epsilon ($\sim 2.5 - 5\epsilon_0$), there is significant scatter away from the inverse relationship, suggesting that other physical variables become can dominate for materials with low electronic polarizability. In Fig. 1(c), a weak positive relationship can be seen between the ZPR and ionicity as measured by the difference in electronegativities ($\Delta\chi$). The Pearson correlation parameter, which ranges form 1.0 (for a perfect positive correlation) and zero (no correlation), allows us to quantify these relationships. The Pearson coefficients are 0.47, 0.51, and 0.33 for E_g, $\frac{1}{\epsilon}$, and $\Delta\chi$, respectively, indicating an imperfect correlation.

To better understand the relationship between simple physical parameters and renormalization, we consider the five structures shown in Fig. 1(d) in detail. We define nine parameters in Table I that we expect to impact the renormalization based on Eqs. (1) and (2) as explained earlier. We prioritize features that are relatively easy to compute.

(1) E_g: Calculated band gap of a material without phonon-induced renormalization.

(2) ϵ_∞^{2D}: Calculated mean in-plane electronic dielectric constant of the material.

(3) $\Delta\chi$: Maximum difference in the Pauling electronegativity between any two atoms in the system.

(4) Δ_Z^*: Maximum difference in Born effective charges between any two atoms in the system.

(5) $\overline{N}$: Number of atoms per area.

(6) ρ_{2D}: Total mass of atoms per area.

(7) $\overline{M}$: Mean atomic mass of the system.

(8) $\overline{\omega}$: Mean phonon frequency of the system.

(9) ω_1: Lowest energy optical phonon frequency at $\mathbf{q} = 0$.

We consider both $\Delta\chi$ and Δ_Z^* because they are both a measure of ionicity with different advantages. While Born effective charges describe the atoms within their solid-state environment, they must be calculated from first-principles; on the other hand, Pauling electronegativities are defined for individual atomic species and are available from a table lookup. We also consider different measures of density: $\overline{N}$ and $\overline{M}$.

As shown in Table I, there is some trend between ZPR and the physical parameters considered. Overall, there looks to be either a correlation or inverse correlation between ZPR and E_g, ϵ_∞^{2D}, $\overline{M}$, and $\Delta\chi$. For example, in As_4, a covalently bound material, the bandgap is 0.75 eV and ZPR is 0.04 eV, which is consistent with the expectation that a small band gap and lack of ionicity leads to lower EPH interactions. HfS_2 also shows a small ZPR (0.02 eV) even though it is somewhat ionic ($\Delta\chi = 1.28$) with a larger band gap than As_4 (1.25 eV). While their dielectric constants are nearly equivalent, there is a significant difference in the maximum electronegativity difference across atoms within these materials. This suggests

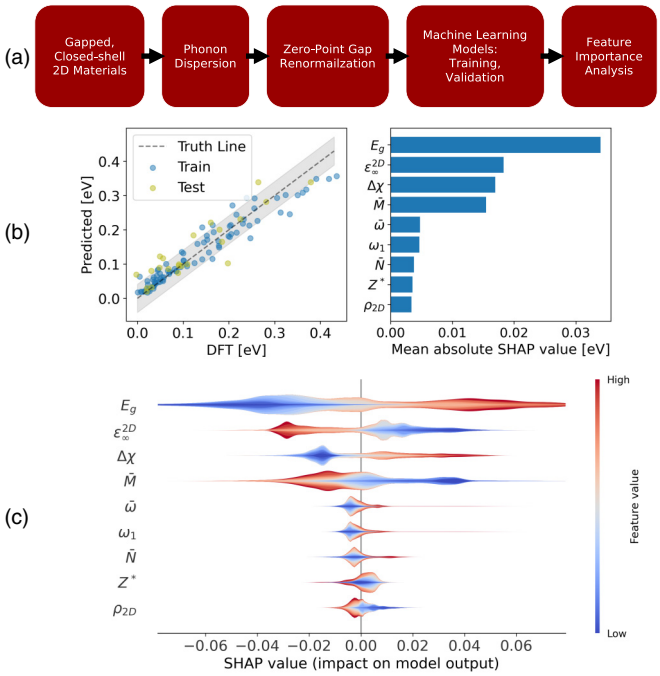

FIG. 2. (a) ML workflow. (b) ERT train and test set accuracy and feature-dependent SHAP values averaged over all materials. The ~95% confidence interval is shown in the shaded region, represented as twice the standard deviation of the residual error. The value for this interval is 60 meV. (c) Violin plot of feature-dependent SHAP values per material. The SHAP value in (b) can be interpreted as the average contribution of each feature to the final ZPR, while the violin plot displays the contribution for each material and illustrates (anti) correlation of the feature with ZPR.

that the sensitivity of the ZPR to differences in electronegativities is not uniform and is likely a nonlinear relationship. This is consistent with other physical variables such as exciton absorption and relative contribution of indirect transitions that depend strongly on the electronegativity difference only over a small range of this difference (<0.2) [66]. For $Mg(OH)_2$, with a DFT band gap of 3.33 eV, a significantly larger ZPR of 0.59 eV is predicted. This material displays some degree of ionicity, a very small mean in-plane dielectric constant ($\epsilon \sim 1$), and small mass density. $MgBr_2$ and MgI_2 have a larger gap but smaller degree of ionicity than $Mg(OH)_2$, with a significantly larger mass density, and a significantly smaller predicted ZPR. Overall, the interdependence of these physical features make it difficult to quantify the relationship between physical parameters and EPH interaction strength as represented by the ZPR.

The workflow for our ML approach is shown in Fig. 2(a). The input DFT data is taken from the work of Mounet and colleagues [42], the SDM is applied, an ML model is fit to the data, and feature importance analysis provides the relationship between physical material properties and renormalization. The model and all predictions can be found in Ref [67].

We utilize the ERT ensemble model with details described in the SM [68]. This ensemble of decision trees is constructed by training individual trees across the entire train data set, but

each point at which a given feature is split is decided randomly instead of per an optimization algorithm [69]. However, by their nature using a single tree is susceptible to overfitting [69,70] where small changes in the input data can produce significantly different trees and thus models that do not generalize well to different sets of input data, which can be alleviated by use of ERT. This is particularly important for small datasets as we have here. Indeed, when we attempted to use a similar spread of methods, we found ERT ensemble models performed best in our use case as well, producing predictive models with a lower ratio between test and train MSE indicative of lower overfitting while maintaining acceptable predictive power. In addition, there is precedent for using such models in similar materials science use cases [41,71–74].

For our model, 80% of the data is used for training and 20% for testing, with the data shown in Fig. 1(b). Figure 2(b) demonstrates the ERT models' predictive capabilities with comparison of the predictions against ground truth. The resulting train root mean square error (RMSE) is 30 meV, with a train score of ∼0.9, while the test RMSE is 43 meV. Additionally, we note that the 95% confidence interval band of the resulting fit is ∼60 meV, i.e., 95% of our predictions lie within this energy distribution to the target value. We consider this value quite narrow given the limitations of our dataset. See SM Secs. IV and V for convergence and accuracy of the ERT model [68].

We note that one metric suggesting that our model has overfitting behavior is the train/test MSE as discussed in the SM [68] and References therein [75]. Theoretically, this ratio should ∼1 as the model learns the relationship present in the data without learning the bias of any particular sample of the data, but our ratio of ∼2.1 suggests predictive performance is stronger on training than holdout data, indicating the bias of our training data is present in the model. However, as discussed in the SM, we utilized hyperparameter optimization to minimize this overfitting problem.

Figure 2(b) shows the most significant independent variables that play a role in the training of the model via a violin plot. Since ensemble tree models are not intrinsically interpretable [76], we choose to use SHAP (Shapley additive explanations) values as an extrinsic tool for statistical interpretability [43,77]. SHAP has been recently utilized to understand structural features that lead to electrocatalysis in N-doped carbon materials [44] and the electronic structure of graphene oxide [78]. Briefly, SHAP trains a given model with every permutation of input features and generates predictions on the data. SHAP then compares the changes in output value when a feature is included versus when not included, calculating the marginal feature contributions and weighs these contributions across every instance of feature inclusion/exclusion. This analysis is sensitive to the number of trees included in the ERT, so we increase the number of trees until we obtain a consistent SHAPLey analysis.

The SHAP value for each feature can be negative (reducing the ZPR) or positive (increasing the ZPR). The most significant four predictors of ZPR and their contributions to the ZPR on average are found to be as follows: (1) DFT gap (34 meV); (2) dielectric constant (18 meV); (3) ionicity as determined from Pauling electronegativies (17 meV); and (4) average mass (15 meV). Interestingly, the difference in electronegativities is significantly more correlated with ZPR than Born effective charges (Δ_Z^*), although both are meant to capture the ionicity of bonds. This is surprising because the Born effective charges are expected to capture the details of ionic polarization more accurately. Additionally, the first optical or averaged optical phonon frequencies contribute almost the exact same amount to the ZPR, both being much less significant than the average mass of atoms. While phonon frequencies are related to the inverse of the reduced mass, the mass also plays a role in the electronic structure and hence, may be the more important feature.

Figure 2(c) shows the violin plot of the SHAP value for every material used in the training of the ML model, with the relative value of the feature shown in the color bar. From this plot, we see visually the correlations between physical parameters and ZPR as determined by the ML model. Here, blue (red) indicate a low (high) feature value, for the positive or negative contribution on the ZPR prediction indicated along the plot's y-axis. We find that the SHAP relationships follow the physical intuition discussed above. For example, a larger gap (indicated by red E_g values) leads to a larger positive contribution to ZPR (positive along the y-axis), while smaller gap values (blue E_g values) lead to a negative contribution to the ZPR (negative on the y-axis). Ionicity represented by Δ_χ shows similar behavior to the gap while ϵ_∞^{2D} inversely correlates; i.e., as the dielectric constant increases, the contribution to ZPR goes towards negative values. Similarly, while phonon frequency correlates with the ZPR, the mass inversely correlates as expected. We also tested LASSO-LSF approach [79] to combine our features into one feature vector and did not find considerable improvement in the accuracy of the model. However, we note that the important feature vectors predicted by LASSO-SF are consistent with our ERT-SHAP analysis (see SM Sec. IIIC) [68].

We use the fact that many of the features are interdependent to select fewer, easily calculable features to develop a more easily applicable model, extending the potential of our model for material search. We consider only E_g, $\overline{N}$, $\overline{M}$, Δ_χ, and $\overline{M}$ and refit our model with only the gap calculated from DFT. As for the full model, we use cross-validation to select optimal parameters, and validate the model on an 80–20 train-test split. The refit model applied to 113 materials results in slightly higher RMSE (train: 53 meV; test: 45 meV) but a reduction in overfitting (test/train ratio ∼0.7). We then applied these optimally selected parameters and retrained our model with the original data set plus 15 additional high-gap materials, taken from the C2dB database [49,80] to address the model's deficiencies in the very high (> 0.5) ZPR range. Finally, we applied this model to predict the ZPR for ∼1302 2D materials from C2dB (see Ref. [68] and supporting documents).

We test the ML prediction by comparison to DFT/SDM-predicted ZPR for five randomly selected materials: $CaCl_2$, Ge_2O_2, $InGaS_2$, SbSeBr, and ZrSSe. As shown in Table S3 and Fig. 3(b), the ML predicts low ZPR values in excellent agreement with PBE. For the more strongly renormalized materials, $CaCl_2$ and Ge_2O_2, the ML model underestimates ZPR because of the sparsity of data at those higher values, leading to a less accurate description. Importantly, the trends

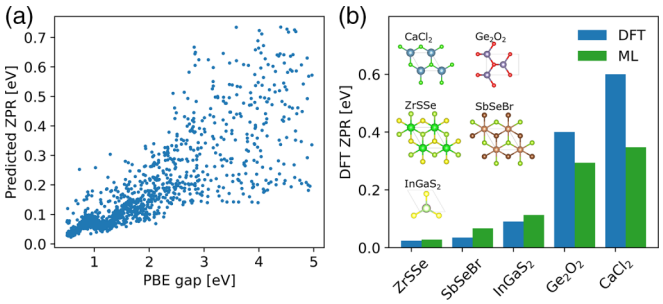

FIG. 3. (a) Predicted ZPR as a function of DFT-PBE bandgap for 1302 materials from the C2DB database. (b) Comparison of ML and DFT-predicted ZPR five randomly selected materials studied.

among the five materials are well predicted by the ML, indicating that our model provides a good estimate of different renormalization regimes for little computational cost just by knowing simple physical parameters. We expect that this is particularly significant in distinguishing materials within high and low electron-phonon coupling regimes.

In summary, we presented a high-throughput study of the band gap ZPR within 2D materials, utilizing the special displacement method to calculate ZPR at low computational cost. We trained an ERT model on physically motivated properties of the materials in the database in order to analyze the relative importance of different physical observables for the prediction of ZPR and found that the bandgap, in-plane dielectric constant, degree of ionicity, and average mass of atoms are the most significant features. Additionally, we trained a reduced-feature ERT model, trained only on features that require either no calculation or an inexpensive DFT calculation on a unit cell. This is important because the model can be applied to large databases of materials in order to differentiate regimes for renormalization for high-throughput screening, something that would not be possible from first-principles. This enables the identification of materials demonstrating exceptionally strong EPH couplings, facilitating, for example, predictions of potential manifestations of polaronic effects [6]. In future work, it will be interesting to explore how correlation effects beyond DFT-PBE affect the phonon-induced band gap renormalization and the exciton binding energy [81]. Furthermore, the inclusion of nonadiabatic effects [14,54], long-range Fröhlich couplings [20], tadpole self-energy corrections [56,57], and anharmonicity [82–86], which are more complex terms to be amenable to high-throughput machine learning approaches, holds promise as topics of future research. The results of the present study constitute an excellent basis for achieving improved predictions in this respect.

Acknowledgments. We acknowledge financial support from the U.S. Department of Energy (DOE), Office of Science, Basic Energy Sciences under Award No. DE-SC0023402. We would like to acknowledge computational resources from the Shared Computing Cluster, which is administered by Boston University's Research Computing located at the Massachusetts Green High Performing Center (MGHPC) and the National Energy Research Scientific Computing Center (NERSC), a DOE Office of Science User Facility supported by the Office of Science of the U.S. Department of Energy under Contract No. DE-AC02-05CH11231, and HPC resources from the Texas Advanced Computing Center (TACC) at The University of Texas at Austin [87]. F.G. is supported by the Computational Materials Sciences Program funded by the U.S. Department of Energy, Office of Science, Basic Energy Sciences, under Award No. DE-SC0020129. M.Z. was funded by the European Union (ULTRA-2DPK / HORIZON-MSCA-2022-PF-01 / Grant Agreement No. 101106654). Views and opinions expressed are however those of the authors only and do not necessarily reflect those of the European Union or the European Commission. Neither the European Union nor the granting authority can be held responsible for them.

[1] M. M. Ugeda, A. J. Bradley, S.-F. Shi, F. H. Da Jornada, Y. Zhang, D. Y. Qiu, W. Ruan, S.-K. Mo, Z. Hussain, Z.-X. Shen, F. Wang, S. G. Louie, and M. F. Crommie, Giant bandgap renormalization and excitonic effects in a monolayer transition metal dichalcogenide semiconductor, Nat. Mater. **13**, 1091 (2014).

[2] A. Arora, K. Nogajewski, M. Molas, M. Koperski, and M. Potemski, Exciton band structure in layered $MoSe_2$: From a monolayer to the bulk limit, Nanoscale **7**, 20769 (2015).

[3] A. Arora, M. Koperski, K. Nogajewski, J. Marcus, C. Faugeras, and M. Potemski, Excitonic resonances in thin films of WSe_2 : From monolayer to bulk material, Nanoscale **7**, 10421 (2015).

[4] D. Y. Qiu, F. H. da Jornada, and S. G. Louie, Screening and many-body effects in two-dimensional crystals: Monolayer MoS_2, Phys. Rev. B **93**, 235435 (2016).

[5] F. Karsai, M. Humer, E. Flage-Larsen, P. Blaha, and G. Kresse, Effects of electron-phonon coupling on absorption spectrum: K edge of hexagonal boron nitride, Phys. Rev. B **98**, 235205 (2018).

[6] W. H. Sio and F. Giustino, Polarons in two-dimensional atomic crystals, Nat. Phys. **19**, 629 (2023).

[7] J. Cao, Y. Wu, H. Zhang, D. Logoteta, S. Zhang, and M. Pala, Dissipative transport and phonon scattering suppression via valley engineering in single-layer antimonene and arsenene field-effect transistors, npj 2D Mater. Appl. **5**, 59 (2021).

[8] L. Wang, Z. Tian, B. Zhang, B. Xu, T. Wang, Y. Wang, S. Li, Z. Di, and Y. Mei, On-chip rolling design for controllable strain engineering and enhanced photon–phonon interaction in graphene, Small **15**, 1805477 (2019).

[9] X. Xu, J. Chen, and B. Li, Phonon thermal conduction in novel 2D materials, J. Phys.: Condens. Matter **28**, 483001 (2016).

[10] A. Afzalian, E. Akhoundi, G. Gaddemane, R. Duflou, and M. Houssa, Advanced DFT–NEGF transport techniques for novel 2-D material and device exploration including HfS_2/WSe_2 van der Waals heterojunction TFET and WTe_2/WS_2 metal/semiconductor contact, IEEE Trans. Electron Devices **68**, 5372 (2021).

[11] Z. Bai, D. He, S. Fu, Q. Miao, S. Liu, M. Huang, K. Zhao, Y. Wang, and X. Zhang, Recent progress in electron–phonon interaction of two-dimensional materials, Nano Select **3**, 1112 (2022).

[12] J. Noffsinger, E. Kioupakis, C. G. Van de Walle, S. G. Louie, and M. L. Cohen, Phonon-assisted optical absorption in silicon from first principles, Phys. Rev. Lett. **108**, 167402 (2012).

[13] G. Antonius, S. Poncé, P. Boulanger, M. Côté, and X. Gonze, Many-body effects on the zero-point renormalization of the band structure, Phys. Rev. Lett. **112**, 215501 (2014).

[14] S. Poncé, Y. Gillet, J. Laflamme Janssen, A. Marini, M. Verstraete, and X. Gonze, Temperature dependence of the electronic structure of semiconductors and insulators, J. Chem. Phys. **143**, 102813 (2015).

[15] M. Zacharias, C. E. Patrick, and F. Giustino, Stochastic approach to phonon-assisted optical absorption, Phys. Rev. Lett. **115**, 177401 (2015).

[16] M. Zacharias and F. Giustino, One-shot calculation of temperature-dependent optical spectra and phonon-induced band-gap renormalization, Phys. Rev. B **94**, 075125 (2016).

[17] F. Giustino, Electron-phonon interactions from first principles, Rev. Mod. Phys. **89**, 015003 (2017).

[18] C. E. P. Villegas, A. R. Rocha, and A. Marini, Electron-phonon scattering effects on electronic and optical properties of orthorhombic GeS, Phys. Rev. B **94**, 134306 (2016).

[19] B. Monserrat, Electron–phonon coupling from finite differences, J. Phys.: Condens. Matter **30**, 083001 (2018).

[20] J. P. Nery, P. B. Allen, G. Antonius, L. Reining, A. Miglio, and X. Gonze, Quasiparticles and phonon satellites in spectral functions of semiconductors and insulators: Cumulants applied to the full first-principles theory and the Fröhlich polaron, Phys. Rev. B **97**, 115145 (2018).

[21] F. Paleari, H. P. C. Miranda, A. Molina-Sánchez, and L. Wirtz, Exciton-phonon coupling in the ultraviolet absorption and emission spectra of bulk hexagonal boron nitride, Phys. Rev. Lett. **122**, 187401 (2019).

[22] E. Cannuccia, B. Monserrat, and C. Attaccalite, Theory of phonon-assisted luminescence in solids: Application to hexagonal boron nitride, Phys. Rev. B **99**, 081109(R) (2019).

[23] S. Reichardt and L. Wirtz, Nonadiabatic exciton-phonon coupling in Raman spectroscopy of layered materials, Sci. Adv. **6**, eabb5915 (2020).

[24] A. Migdal, Interaction between electrons and lattice vibrations in a normal metal, Sov. Phys. JETP **34**, 996 (1958).

[25] G. Antonius, Y.-H. Chan, and S. G. Louie, Polaron spectral properties in doped ZnO and $SrTiO_3$ from first principles, Phys. Rev. Res. **2**, 043296 (2020).

[26] A. Kundu, M. Govoni, H. Yang, M. Ceriotti, F. Gygi, and G. Galli, Quantum vibronic effects on the electronic properties of solid and molecular carbon, Phys. Rev. Mater. **5**, L070801 (2021).

[27] A. M. Alvertis and E. A. Engel, Importance of vibrational anharmonicity for electron-phonon coupling in molecular crystals, Phys. Rev. B **105**, L180301 (2022).

[28] A. M. Alvertis, J. B. Haber, E. A. Engel, S. Sharifzadeh, and J. B. Neaton, Phonon-induced localization of excitons in molecular crystals from first principles, Phys. Rev. Lett. **130**, 086401 (2023).

[29] A. Marini, *Ab initio* finite-temperature excitons, Phys. Rev. Lett. **101**, 106405 (2008).

[30] M. Zacharias and F. Giustino, Theory of the special displacement method for electronic structure calculations at finite temperature, Phys. Rev. Res. **2**, 013357 (2020).

[31] F. Karsai, M. Engel, E. Flage-Larsen, and G. Kresse, Electron–phonon coupling in semiconductors within the GW approximation, New J. Phys. **20**, 123008 (2018).

[32] G. Samsonidze and B. Kozinsky, Accelerated screening of thermoelectric materials by first-principles computations of electron–phonon scattering, Adv. Energy Mater. **8**, 1800246 (2018).

[33] R. Li, E. Lee, and T. Luo, Physics-informed deep learning for solving coupled electron and phonon Boltzmann transport equations, Phys. Rev. Appl. **19**, 064049 (2023).

[34] Y. Zhong, Z. Tao, W. Chu, X. Gong, and H. Xiang, Accelerating the calculation of electron-phonon coupling by machine learning methods, arXiv:2302.00439.

[35] Z. Alizadeh and M. Mohammadizadeh, Predicting electron-phonon coupling constants of superconducting elements by machine learning, Physica C: Supercond. Appl. **558**, 7 (2019).

[36] S. R. Xie, G. R. Stewart, J. J. Hamlin, P. J. Hirschfeld, and R. G. Hennig, Functional form of the superconducting critical temperature from machine learning, Phys. Rev. B **100**, 174513 (2019).

[37] S. R. Xie, Y. Quan, A. C. Hire, B. Deng, J. M. DeStefano, I. Salinas, U. S. Shah, L. Fanfarillo, J. Lim, J. Kim, G. R. Stewart, J. J. Hamlin, P. J. Hirschfeld, and R. G. Hennig, Machine learning of superconducting critical temperature from Eliashberg theory, npj Comput. Mater. **8**, 14 (2022).

[38] G. Zhou, W. Chu, and O. V. Prezhdo, Structural deformation controls charge losses in $MAPbI_3$: Unsupervised machine learning of nonadiabatic molecular dynamics, ACS Energy Lett. **5**, 1930 (2020).

[39] C. Kim, G. Pilania, and R. Ramprasad, Machine learning assisted predictions of intrinsic dielectric breakdown strength of ABX_3 perovskites, J. Phys. Chem. C **120**, 14575 (2016).

[40] S. Bang, J. Kim, D. Wee, G. Samsonidze, and B. Kozinsky, Estimation of electron-phonon coupling via moving least squares averaging: A method for fast-screening potential thermoelectric materials, Mater. Today Phys. **6**, 22 (2018).

[41] J. Schmidt, J. Shi, P. Borlido, L. Chen, S. Botti, and M. A. Marques, Predicting the thermodynamic stability of solids combining density functional theory and machine learning, Chem. Mater. **29**, 5090 (2017).

[42] N. Mounet, M. Gibertini, P. Schwaller, D. Campi, A. Merkys, A. Marrazzo, T. Sohier, I. E. Castelli, A. Cepellotti, G. Pizzi, and N. Marzari, Two-dimensional materials from high-throughput computational exfoliation of experimentally known compounds, Nat. Nanotechnol. **13**, 246 (2018).

[43] S. M. Lundberg and S.-I. Lee, A unified approach to interpreting model predictions, in *Advances in Neural Information Processing Systems*, edited by I. Guyon, U. V. Luxburg, S. Bengio, H. Wallach, R. Fergus, S. Vishwanathan, and R. Garnett (Curran Associates, Inc., 2017), Vol. 30.

[44] S. Tan, R. Wang, G. Song, S. Qi, K. Zhang, Z. Zhao, and Q. Yin, Machine learning and shapley additive explanation-based interpretable prediction of the electrocatalytic performance of N-doped carbon materials, Fuel **355**, 129469 (2024).

[45] K. Morita, D. W. Davies, K. T. Butler, and A. Walsh, Modeling the dielectric constants of crystals using machine learning., J. Chem. Phys. **153**, 024503 (2020).

[46] N. R. Knøsgaard and K. S. Thygesen, Representing individual electronic states for machine learning GW band structures of 2D materials, Nat. Commun. **13**, 468 (2022).

[47] R. Kumar and A. K. Singh, Chemical hardness-driven interpretable machine learning approach for rapid search of photocatalysts, npj Comput. Mater. **7**, 197 (2021).

[48] V. V. Korolev, A. Mitrofanov, E. I. Marchenko, N. N. Eremin, V. Tkachenko, and S. N. Kalmykov, Transferable and extensible machine learning-derived atomic charges for modeling hybrid nanoporous materials, Chem. Mater. **32**, 7822 (2020).

[49] M. N. Gjerding, A. Taghizadeh, A. Rasmussen, S. Ali, F. Bertoldo, T. Deilmann, N. R. Knøsgaard, M. Kruse, A. H. Larsen, S. Manti, T. G. Pedersen, U. Petralanda, T. Skovhus, M. K. Svendsen, J. J. Mortensen, T. Olsen, and K. S. Thygesen, Recent progress of the computational 2D materials database (C2DB), 2D Mater. **8**, 044002 (2021).

[50] T. Huang, D. K. Lewis, and S. Sharifzadeh, Assessing the role of intermolecular interactions in a perylene-based nanowire using first-principles many-body perturbation theory, J. Phys. Chem. Lett. **10**, 2842 (2019).

[51] T. A. Huang, M. Zacharias, D. K. Lewis, F. Giustino, and S. Sharifzadeh, Exciton–phonon interactions in monolayer germanium selenide from first principles, J. Phys. Chem. Lett. **12**, 3802 (2021).

[52] P. B. Allen and V. Heine, Theory of the temperature dependence of electronic band structures, J. Phys. C **9**, 2305 (1976).

[53] F. Giustino, S. G. Louie, and M. L. Cohen, Electron-phonon renormalization of the direct band gap of diamond, Phys. Rev. Lett. **105**, 265501 (2010).

[54] A. Miglio, V. Brousseau-Couture, E. Godbout, G. Antonius, Y.-H. Chan, S. G. Louie, M. Côté, M. Giantomassi, and X. Gonze, Predominance of non-adiabatic effects in zero-point renormalization of the electronic band gap, npj Comput. Mater. **6**, 167 (2020).

[55] M. Zacharias, M. Scheffler, and C. Carbogno, Fully anharmonic nonperturbative theory of vibronically renormalized electronic band structures, Phys. Rev. B **102**, 045126 (2020).

[56] J. Lafuente-Bartolome, C. Lian, W. H. Sio, I. G. Gurtubay, A. Eiguren, and F. Giustino, Unified approach to polarons and phonon-induced band structure renormalization, Phys. Rev. Lett. **129**, 076402 (2022).

[57] J. Lafuente-Bartolome, C. Lian, W. H. Sio, I. G. Gurtubay, A. Eiguren, and F. Giustino, *Ab initio* self-consistent many-body theory of polarons at all couplings, Phys. Rev. B **106**, 075119 (2022).

[58] W. H. Sio and F. Giustino, Unified *ab initio* description of Fröhlich electron-phonon interactions in two-dimensional and three-dimensional materials, Phys. Rev. B **105**, 115414 (2022).

[59] P. Giannozzi, S. Baroni, N. Bonini, M. Calandra, R. Car, C. Cavazzoni, D. Ceresoli, G. L. Chiarotti, M. Cococcioni, I. Dabo, A. Dal Corso, S. De Gironcoli, S. Fabris, G. Fratesi, R. Gebauer, U. Gerstmann, C. Gougoussis, A. Kokalj, M. Lazzeri, L. Martin-Samos *et al.*, QUANTUM ESPRESSO: A modular and open-source software project for quantum simulations of materials, J. Phys.: Condens. Matter **21**, 395502 (2009).

[60] P. Giannozzi, O. Baseggio, P. Bonfà, D. Brunato, R. Car, I. Carnimeo, C. Cavazzoni, S. De Gironcoli, P. Delugas, F. Ferrari Ruffino, A. Ferretti, N. Marzari, I. Timrov, A. Urru, and S. Baroni, QUANTUM ESPRESSO toward the exascale, J. Chem. Phys. **152**, 154105 (2020).

[61] G. Prandini, A. Marrazzo, I. E. Castelli, N. Mounet, and N. Marzari, Precision and efficiency in solid-state pseudopotential calculations, npj Comput. Mater. **4**, 72 (2018).

[62] P. Giannozzi, O. Andreussi, T. Brumme, O. Bunau, M. Buongiorno Nardelli, M. Calandra, R. Car, C. Cavazzoni, D. Ceresoli, M. Cococcioni, N. Colonna, I. Carnimeo, A. Dal Corso, S. De Gironcoli, P. Delugas, R. A. DiStasio, A. Ferretti, A. Floris, G. Fratesi, G. Fugallo *et al.*, Advanced capabilities for materials modelling with Quantum ESPRESSO, J. Phys.: Condens. Matter **29**, 465901 (2017).

[63] J. P. Perdew, K. Burke, and M. Ernzerhof, Generalized gradient approximation made simple, Phys. Rev. Lett. **77**, 3865 (1996).

[64] P. Y. Yu and M. Cardona, *Fundamentals of Semiconductors. Physics and Materials Properties*, 4th ed. (Springer, 2010).

[65] M. L. Cohen and S. G. Louie, *Fundamentals of Condensed Matter Physics* (Cambridge University Press, Cambridge, 2016).

[66] G. D. Mahan, *Condensed Matter in a Nutshell*, In a Nutshell (Princeton University Press, Princeton, NJ, 2011).

[67] 2D Materials ZG Inference Example Notebook, https://github.com/fpmats/htzg_ml/blob/main/ml_inference_example.ipynb.

[68] See Supplemental Materials at http://link.aps.org/supplemental/10.1103/PhysRevMaterials.8.L101001 for DFT and ML computational details, alternative machine learning models, and limitations of the extra random trees model.

[69] P. Geurts, D. Ernst, and L. Wehenkel, Extremely randomized trees, Mach. Learn. **63**, 3 (2006).

[70] P. R. Cohen and D. Jensen, Overfitting explained, in *Sixth International Workshop on Artificial Intelligence and Statistics* (PMLR, 1997), pp. 115–122.

[71] J. Schmidt, M. R. Marques, S. Botti, and M. A. Marques, Recent advances and applications of machine learning in solid-state materials science, npj Comput. Mater. **5**, 83 (2019).

[72] T. Toyao, K. Suzuki, S. Kikuchi, S. Takakusagi, K.-i. Shimizu, and I. Takigawa, Toward effective utilization of methane: Machine learning prediction of adsorption energies on metal alloys, J. Phys. Chem. C **122**, 8315 (2018).

[73] M. A. Shandiz and R. Gauvin, Application of machine learning methods for the prediction of crystal system of cathode materials in lithium-ion batteries, Comput. Mater. Sci. **117**, 270 (2016).

[74] Y. Zhang and C. Ling, A strategy to apply machine learning to small datasets in materials science, npj Comput. Mater. **4**, 25 (2018).

[75] M. Belkin, D. Hsu, S. Ma, and S. Mandal, Reconciling modern machine-learning practice and the classical bias–variance trade-off, Proc. Natl. Acad. Sci. USA **116**, 15849 (2019).

[76] S. Yan, S. Natarajan, S. Joshi, R. Khardon, and P. Tadepalli, Explainable models via compression of tree ensembles, arXiv:2206.07904.

[77] S. M. Lundberg, G. Erion, H. Chen, A. DeGrave, J. M. Prutkin, B. Nair, R. Katz, J. Himmelfarb, N. Bansal, and S.-I. Lee, From local explanations to global understanding with explainable AI for trees, Nat. Mach. Intell. **2**, 56 (2020).

[78] A. S. Barnard and B. L. Fox, Importance of structural features and the influence of individual structures of graphene oxide using Shapley value analysis, Chem. Mater. **35**, 8840 (2023).

[79] C. Kim, G. Pilania, and R. Ramprasad, From organized high-throughput data to phenomenological theory using machine learning: the example of dielectric breakdown, Chem. Mater. **28**, 1304 (2016).

[80] S. Haastrup, M. Strange, M. Pandey, T. Deilmann, P. S. Schmidt, N. F. Hinsche, M. N. Gjerding, D. Torelli, P. M. Larsen, A. C. Riis-Jensen, J. Gath, K. W. Jacobsen, J. Jørgen Mortensen, T. Olsen, and K. S. Thygesen, The computational 2D materials database: High-throughput modeling and discovery of atomically thin crystals, 2D Mater. **5**, 042002 (2018).

[81] Z. Jiang, Z. Liu, Y. Li, and W. Duan, Scaling universality between band gap and exciton binding energy of two-dimensional semiconductors, Phys. Rev. Lett. **118**, 266401 (2017).

[82] O. Hellman, I. A. Abrikosov, and S. I. Simak, Lattice dynamics of anharmonic solids from first principles, Phys. Rev. B **84**, 180301(R) (2011).

[83] I. Errea, M. Calandra, and F. Mauri, Anharmonic free energies and phonon dispersions from the stochastic self-consistent harmonic approximation: Application to platinum and palladium hydrides, Phys. Rev. B **89**, 064302 (2014).

[84] T. Tadano and S. Tsuneyuki, Self-consistent phonon calculations of lattice dynamical properties in cubic $SrTiO_3$ with first-principles anharmonic force constants, Phys. Rev. B **92**, 054301 (2015).

[85] L. Monacelli, R. Bianco, M. Cherubini, M. Calandra, I. Errea, and F. Mauri, The stochastic self-consistent harmonic approximation: Calculating vibrational properties of materials with full quantum and anharmonic effects, J. Phys.: Condens. Matter **33**, 363001 (2021).

[86] M. Zacharias, G. Volonakis, F. Giustino, and J. Even, Anharmonic lattice dynamics via the special displacement method, Phys. Rev. B **108**, 035155 (2023).

[87] http://www.tacc.utexas.edu